

# Solidification and epitaxial regrowth in surface nanostructuring with laser-assisted scanning tunneling microscope

Xinwei Wang<sup>a)</sup>

*Department of Mechanical Engineering, N104 Walter Scott Engineering Center, The University of Nebraska-Lincoln, Lincoln, Nebraska 68588-0656*

Yongfeng Lu

*Department of Electrical Engineering, 209N Walter Scott Engineering Center, The University of Nebraska-Lincoln, Lincoln, Nebraska 68588-0511*

(Received 2 June 2005; accepted 17 October 2005; published online 2 December 2005)

In this work, parallel molecular-dynamics simulation is conducted to study the long-time (up to 2 ns) behavior of argon crystal in surface nanostructuring with a laser-assisted scanning tunneling microscope. A large system consisting of more than  $1 \times 10^8$  at. is explored. The study is focused on the solidification procedure after laser irradiation, which is driven by heat conduction in the material. Epitaxial regrowth is observed in the solidification. Atomic dislocation due to thermal strain-induced structural damages is observed as well in epitaxial regrowth. During solidification, the liquid is featured with decaying normal compressive stresses and negligible shear stresses. Two functions are designed to capture the structure and distinguish the solid and liquid regions. These functions work well in terms of reflecting the crystallinity of the material and identifying the atomic dislocations. The study of the movement of the solid-liquid interface reveals an accelerating moving speed in the order of 3–5 m/s. The spatial distribution of the moving speed at the solid-liquid interface indicates a nonuniform epitaxial regrowth in space. The bottom of the liquid solidifies slower than that at the edge. © 2005 American Institute of Physics. [DOI: [10.1063/1.2135416](https://doi.org/10.1063/1.2135416)]

## I. INTRODUCTION

As a maskless, top-down nanofabrication technique, the laser-assisted scanning tunneling microscope (STM) provides a wide variety of potential applications in nanoscience and nanotechnology. Examples of such applications include surface nanorepair, fabrication and characterization of nano-to microscale integrated nanoelectronics and nanophotonics, and machining and aligning of nanoparticles and nanotubes/wires. In surface nanostructuring with laser-assisted STM, the STM tip is irradiated with a laser beam. The STM tip could act as a receiving antenna to collect laser energy and as a transmitting antenna to create a significantly enhanced optical field in proximity to the tip apex. The optical field could be enhanced by two orders of magnitude.<sup>1</sup> Therefore, the enhanced optical field can heat the sample surface below the tip to induce phase change or chemical reaction and modify the surface at nanoscales.<sup>2–12</sup> In the works of Chimmalgi *et al.*<sup>11</sup> and Huang *et al.*,<sup>12</sup> a laser-assisted atomic force microscope (AFM) was used, which plays the same role as the laser-assisted STM in terms of optical-field enhancement. Comprehensive and detailed information on the laser-assisted STM and the involved physical mechanisms can be found in a review by Grafström.<sup>13</sup>

In laser-assisted STM nanostructuring, as a direct consequence of nanoscale heating, the nanodomain of the sample just below the STM tip experiences intense heating, phase change, phase explosion, stress development and propagation, and rapid structural evolution. Because of the small size

(tens of nanometers) of the domain under structuring, continuum approaches may fail to understand and predict the above physical processes. Although a large number of work has been reported to study the enhanced optical field and light confinement,<sup>14–18</sup> only the thermal evolution of the sample surface under the STM tip has been studied for the case without phase change.<sup>19,20</sup> At nanoscales, thermal movements of molecules/atoms will show strong statistical variations in space since thermal equilibrium cannot be well established. Molecular-dynamics (MD) simulation, which directly tracks the movement of molecules/atoms, is capable of exploring the physical phenomena down to molecular/atomic levels. In the recent work of Wang,<sup>21</sup> the thermal, mechanical, and structural phenomena in surface nanostructuring with picosecond laser-assisted STM were studied using large-scale parallel MD simulation. The work is focused on the physical processes during laser heating and within a short time after laser heating (up to 500 ps). In surface nanostructuring, the final surface nanostructure is strongly affected by solidification of the melted material. The solidification process is driven by the heat conduction in the material and is much slower than the heating and melting processes that are largely driven by the laser energy input. To date, little research has been conducted to study the natural solidification in surface nanostructuring with laser-assisted STM. In the past, MD simulation has been conducted on small-scale (several angstroms) solidification in ion-induced damage and annealing of Si (Ref. 22) and solidification in rapid cooling of materials.<sup>23–25</sup> The solidification in surface nanostructuring with laser-assisted STM is driven by heat conduction, which is much slower than the artificially cool-

<sup>a)</sup>Author to whom correspondence should be addressed; FAX: (402) 472-1465; electronic mail: [xwang3@unl.edu](mailto:xwang3@unl.edu)

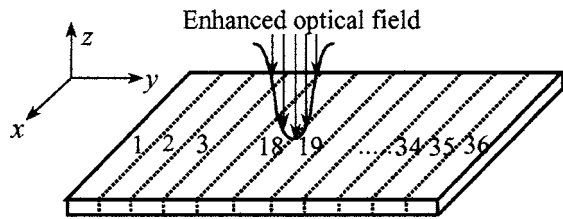


FIG. 1. Schematic of the MD configuration.

ing introduced to the system in some of the previous researches.<sup>23–25</sup> In addition, laser-induced strain and stress<sup>21,26</sup> can have profound impact on the solidification procedure and affect the crystal structure.

In this work, large-scale parallel MD simulations are conducted to study the solidification process in surface nanostructuring with laser-assisted STM. A system consisting of more than  $1 \times 10^8$  at. are modeled up to 2 ns to capture the details of solidification and crystallization. The research is focused on the dynamic behavior of the solid-liquid interface, crystallinity of the regrown crystal, and strain-induced atomic dislocation.

## II. METHODOLOGIES OF SIMULATION

As shown in Fig. 1, a freestanding film is irradiated with an enhanced optical field. Argon at 50 K is chosen for film material for the simplicity of computation. This makes it feasible to study large systems for a long duration and to reveal the fundamental physics involved in solidification. The generic and qualitative conclusions drawn from this work will not be affected by the material itself.

The movement of atoms is governed by the Newtonian equation,

$$m_i \frac{d^2 r_i}{dt^2} = \sum_{j \neq i} F_{ij}, \quad (1)$$

where  $m_i$  and  $r_i$  are the mass and position of atom  $i$ , respectively.  $F_{ij}$  is the interaction force between atoms  $i$  and  $j$ , and is computed from the Lennard-Jones (LJ) potential as  $F_{ij} = -\partial \phi_{ij} / \partial r_{ij}$ . The Lennard-Jones potential  $\phi_{ij}$  follows the form

$$\phi_{ij} = 4\epsilon \left[ \left( \frac{\sigma_e}{r_{ij}} \right)^{12} - \left( \frac{\sigma_e}{r_{ij}} \right)^6 \right], \quad (2)$$

where  $\epsilon$  is the LJ well depth parameter,  $\sigma_e$  is referred to as the equilibrium separation parameter, and  $r_{ij} = r_i - r_j$ .

In our work, the half-step leap-frog scheme is used.<sup>27</sup> The interaction between atoms is neglected when their distance exceeds a particular length  $r_c$ , namely, the cutoff distance. For argon, the widely accepted value of  $2.5\sigma_e$  for  $r_c$  is adopted. Computation of the force between an atom and its neighbors is arranged by the cell structure and the linked-list methods.<sup>27</sup> More details about the computation can be found in the work of Wang.<sup>21</sup>

Parallel computation is employed in this work. In the  $y$  direction, the physical domain is divided into 36 subdomains of the same size as shown in Fig. 1. These subdomains are distributed over a superparallel computer consisting of 36

TABLE I. Values of the parameters used in the simulation.

Parameter	Value
$\epsilon$ , LJ well depth parameter	$1.653 \times 10^{-21}$ J
$\sigma_e$ , LJ equilibrium separation	3.406 Å
$m$ , argon atomic mass	$66.3 \times 10^{-27}$ kg
$k_B$ , Boltzmann's constant	$1.38 \times 10^{-23}$ J/K
$a$ , lattice constant	5.414 Å
$r_c$ , cutoff distance	8.515 Å
$\tau$ , laser beam absorption depth	10 nm
$\delta t$ , time step	25 fs
$I_0$	$1.5325 \times 10^{12}$ W/m <sup>2</sup>
$r_g$	25 nm
$t_0$	10 ps
$t_g$	3 ps

computing nodes. Each node is responsible for the MD simulation of one subdomain. The parallel program is developed using MPICH. Details of the parallel treatment are discussed in our recent work.<sup>28</sup>

The distribution of the optical field in space and time domains takes the form of

$$I = I_0 \exp[-(\mathbf{r} - \mathbf{r}_0)^2 / r_g^2] \exp[-(t - t_0)^2 / t_g^2], \quad (3)$$

where  $I_0$  is a laser beam intensity constant,  $\mathbf{r}$  is the location of the laser beam,  $\mathbf{r}_0$  is the center of the sample surface,  $r_g$  is a length constant determining the size of the laser beam,  $t$  is the time,  $t_0$  is a time constant determining the peak location of the laser intensity in the time domain, and  $t_g$  is a time constant determining the pulse width of the laser beam. The laser beam distribution in Eq. (3) is constructed for the convenience of computing. Values of these parameters are summarized in Table I. The simulation reported in this work is for generic situations, and no specific wavelength of the laser beam is used. Therefore, an artificial optical-absorption depth ( $\tau$ ) of 10 nm is taken in the simulation. This optical-absorption depth is chosen to reflect the fact of volumetric absorption of the laser beam in the sample rather than a practical experimental condition. It needs to be pointed out that surface nanostructure fabricated using laser-assisted STM can be strongly affected by the wavelength of the laser beam. This is because the wavelength of the laser beam can significantly affect the laser-STM tip interaction, thereby varying the intensity and spacial distribution of the enhanced optical field. Furthermore, laser beam absorption in the substrate material is strongly dependent on the wavelength of the laser beam. Different wavelengths will lead to different absorption depths, resulting in varied surface nanostructures.

Figure 2 shows how the laser energy absorption is achieved in the modeling. The MD domain is divided into cubic cells, whose size is a little larger than the cutoff distance. Cell 1 is taken as the example to show how the laser beam absorption is treated. The laser energy incident on cell 1 within each time step ( $\delta t$ ) is  $E_1 = \int_A I \delta t \cdot dA$ , where  $A$  is the top surface area of cell 1. Within each time step, the laser energy absorbed in cell 1 is

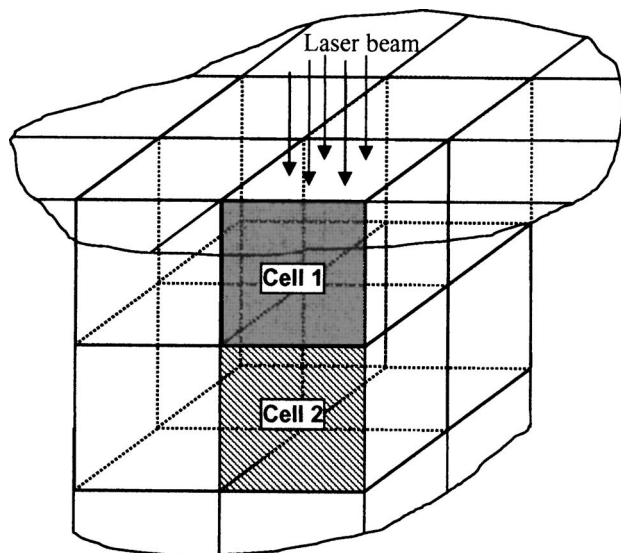


FIG. 2. Schematic of the laser beam absorption treatment in the material.

$$\delta E_1 = E_1[1 - \exp(-\delta z/\tau_1)], \quad (4)$$

where  $\delta z$  is the size of cell 1 in the  $z$  direction. This laser beam absorption is realized by adjusting the velocity of atoms in cell 1 with a factor. The real optical-absorption depth of cell 1 is adjusted to be  $\tau_1 = \tau \cdot \rho_0 / \rho_1$  with  $\rho_1$  the density of atoms in cell 1 and  $\rho_0$  the density of argon at 50 K. The velocity scaling needs to be constructed to meet the requirement of momentum conservation to avoid physically unreasonable atom movement. Details of the velocity scaling are discussed in the work of Wang.<sup>21</sup>

After passing cell 1, the incident laser energy on cell 2 will be  $E_2 = E_1 - \delta E_1$ . Then the aforementioned procedure is repeated to calculate the laser beam absorption in cell 2. The same laser beam absorption treatment is applied to cells in other areas of the MD domain.

### III. RESULTS AND DISCUSSION

In this work, a target comprised of 648 fcc unit cells (350.83 nm) in the  $x$  and  $y$  directions and 60 fcc unit cells (32.48 nm) in the  $z$  direction is simulated. The sample is constructed to have its length much larger than the beam spot ( $\sim 25$  nm), and its thickness much longer than the optical-absorption depth (10 nm). The pulse energy is taken as  $8 \times 10^{-15}$  J, which corresponds to an energy density level of 50 MW/cm<sup>2</sup>. As indicated in Table I, the spatial distribution of the laser pulse is assumed to have a radius of 25 nm at  $e^{-1}$  of the peak intensity. The corresponding beam spot is much smaller than the typical wavelength of picosecond lasers. In a laser-assisted STM, the STM tip could act as a receiving antenna to collect laser energy and as a transmitting antenna to create a significantly enhanced optical field in proximity to the tip apex. Previous theoretical calculations<sup>1</sup> showed that the enhanced optical field was confined within a small domain in the order of tens of nanometers. Therefore, the laser-assisted STM makes it possible to focus the laser beam to a spot much smaller than the laser wavelength.

Before applying laser heating, the simulation is run for 100 ps (4000 steps) (1 ps =  $10^{-12}$  s), during which the veloc-

ity of atoms is scaled to make the sample to reach 50 K gradually. After this velocity scaling, the sample is simulated for another 100 ps (4000 steps) to eliminate the disturbance introduced by the velocity scaling. Periodical boundary conditions are applied to the boundaries in the  $x$  and  $y$  directions, and free boundary conditions to the boundaries in the  $z$  direction. Free spaces are added below and above the sample to capture the movement of atoms escaping from the sample. The computational domain measures 350.83 nm in the  $x$  and  $y$  directions, and 759.10 nm in the  $z$  direction with the back side of the sample located at 213.71 nm. A total of 100 776 960 atoms are simulated for this case. Using the 36 computing nodes in our laboratory, it takes about 48.4 s to finish one step. The entire computation until 2 ns takes about 50 days to finish. The data for the velocity and position of the atoms in each computing node are stored on the local hard disk. A parallel postprocessing package was developed to compute the distribution and evolution of various physical parameters, including temperature, stress, velocity, and structure.

#### A. Melting, vaporization, solidification, and epitaxial regrowth

Figure 3 shows the snapshots of atomic positions in an  $x$ - $z$  plane 1.77 nm thick centered at  $y = 174.53$  nm. In these plots, each dot represents an atom. The plots from 5 to 100 ps largely demonstrate the laser-induced heating, melting, and vaporization. At the beginning ( $t = 5$  ps), laser heating is weak, and the sample shows a uniform crystal structure. At 10 ps, the center at the surface becomes dark because the local solid is melted. The random distribution of atoms in this region makes it look dark. At the time the laser stops ( $t = 15$  ps), vapor is observed at the surface of the central part of the sample. On the other hand, the target surface is not much nanostructured. Starting from 20 ps, the melt in the sample starts to explode and a large number of nanodroplets are formed and ejected from the sample. At 100 ps, the explosion process looks much weaker. On the other hand, the liquid surface is not smooth. From 100 to 500 ps, the surface tension makes the liquid surface smooth, and very few droplets are observed at 500 ps. More detailed discussion of the heating, melting, vaporization, and explosion processes for targets of different sizes under different enhanced optical fields is provided in our recent work.<sup>21</sup> In this paper, our interest is the solidification process after laser heating. This process is clearly shown in the plots from 500 ps (0.5 ns) to 2 ns. Comparing the plots at 0.5 and 1 ns, it is evident that the top edge of the liquid in the nanohole solidifies first. Comparison of the plots at 0.5 and 2 ns shows that the total volume of the liquid becomes much smaller at 2 ns, indicating a fast solidification procedure in a short time period (1.5 ns). One important phenomenon observed in Fig. 3 is the thermal strain-induced defect in the regrown crystal. This defect (atomic dislocation) is marked in the plot at 2 ns.

To clearly demonstrate the epitaxial regrowth and strain-induced atomic dislocation, we plot out the atomic positions in detail in Fig. 4. It is observed that after regrowth, the crystal follows the crystallographical orientations of the bulk

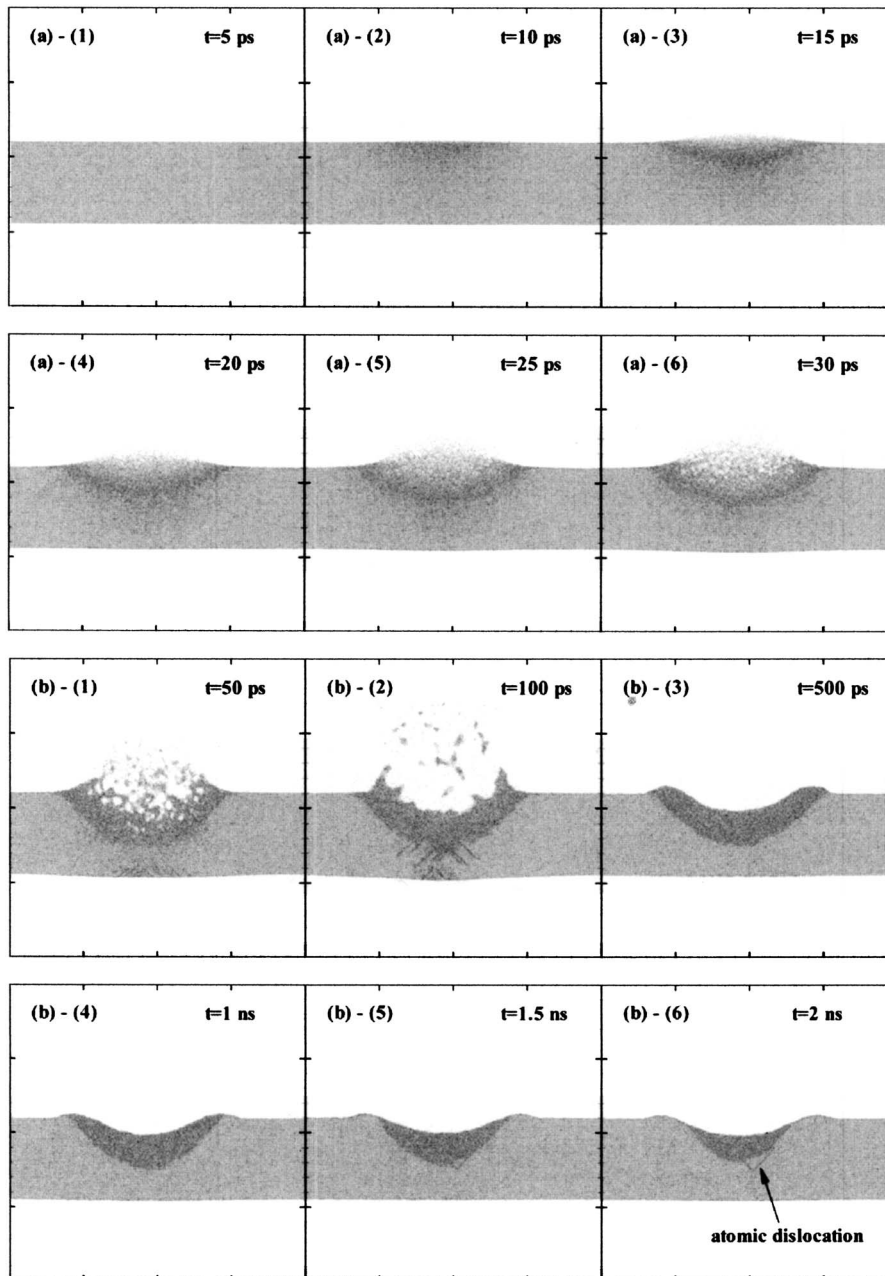


FIG. 3. Snapshots of atomic positions in an  $x$  (horizontal: 120–240 nm)- $z$  (vertical: 180–300 nm) plane 1.77 nm thick centered at  $y=174.53$  nm.

solid, demonstrating epitaxial growth in the solidification. Although the simulation reported in this work is conducted with symmetric boundary conditions, symmetric energy distribution of the laser beam, and uniform material, the strain-induced defect (atomic dislocation) as shown in Fig. 4 is found nonsymmetric. This is because despite the above symmetric conditions used in the simulation, the thermal movement of atoms in space is nonsymmetric and nonuniform. The nonuniformity of the thermal movement of atoms will introduce significant noise to the mechanical behavior of the studied nanoscale system and strongly affects the zone in which atomic dislocation will form. In our previous work,<sup>21</sup> for the same reason, nonsymmetric structural defects and atomic dislocations were also observed during the nanostructuring procedure. It is interesting to note that the orientation of the atomic dislocation region is  $45^\circ$  with respect to the  $z$  direction. This orientation is similar to that of the structural

damages formed during laser heating and thermal stress propagation in laser-assisted STM surface nanostructuring.<sup>21</sup> It is noticed that the shear stress in the material plays the principal role in forming the atomic dislocations. Following  $45^\circ$  with respect to the  $z$  axis, the shear stress induced by the normal stress  $\sigma_{zz}$  in the system has the maximum value. Therefore, atoms are more likely to be dislocated in the direction of  $45^\circ$  with respect to the  $z$  axis.

## B. Thermal and mechanical evolutions

The solidification observed from 0.5 to 2 ns is driven by the heat conduction in the material. In addition, laser-induced stress could affect the solidification procedure to a great extent. This section is intended to study the detailed thermal and mechanical evolutions during the solidification procedure. Figure 5 shows the temperature distribution from 0.6 to

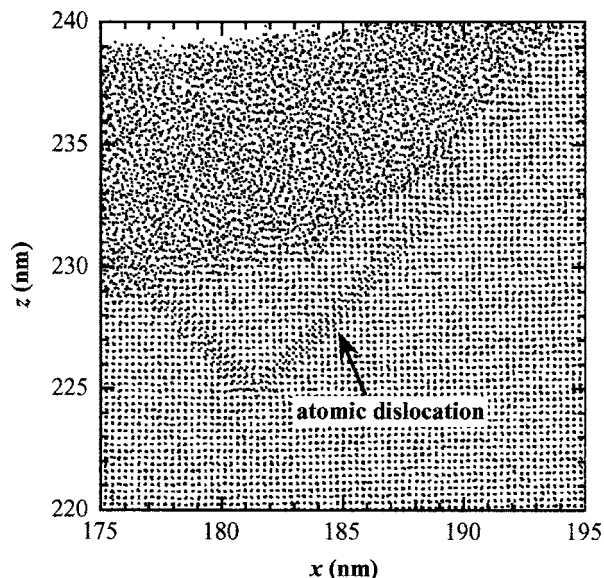


FIG. 4. Details to show the epitaxial growth and atomic dislocation in an  $x$ - $z$  plane 1.77 nm thick centered at  $y=174.53$  nm and  $t=2$  ns.

2 ns in an  $x$ - $z$  plane 1.77 nm thick centered at  $y = 174.53$  nm. At 0.6 ns, the temperature of the melt largely falls in the region of 80–85 K while some areas have a little higher temperature of 85–90 K. Since the melting point of argon is 83.8 K, it is clear that the melted argon in the nanohole is ready to solidify. From 1 to 2 ns, the temperature of the melted argon drops to a level below the melting point because of heat conduction. It means most of the solidification procedure is under a subcooled condition. From the plots shown in Fig. 5, the temperature in the melt is not so uniform, with a spatial roughness of several nanometers. For

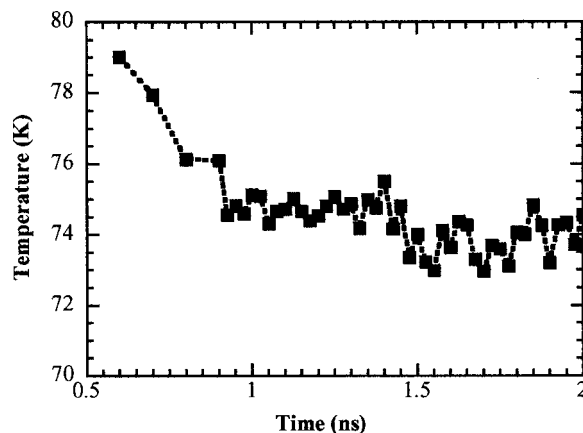


FIG. 6. Evolution of the average temperature of the liquid during the solidification procedure.

macroscale solidification, this temperature nonuniformity may have negligible effect. For the nanoscale solidification studied in this work, it is anticipated that this nanoscale temperature nonuniformity will have profound impact on the epitaxial growth.

To have a clear idea about the temperature evolution of the liquid during solidification, we plot out the average temperature of the liquid versus time in Fig. 6. In the early stage of solidification, the liquid temperature experiences a rapid decay from 79 to 74.5 K within 0.4 ns. Then the liquid temperature decreases slowly with time. One possible explanation for this phenomenon is that in the early stage of solidification, there is a large solid-liquid interface. As a result, the liquid has a large area to transfer the thermal energy to the solid. Therefore, the liquid experiences a rapid cooling. In

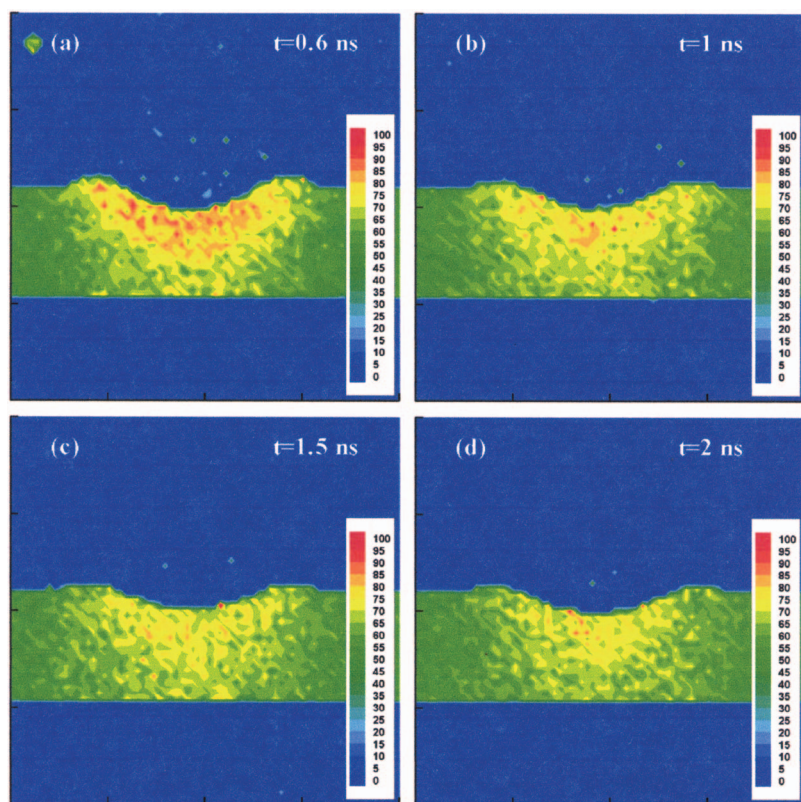


FIG. 5. (Color) Temperature distribution in an  $x$  (horizontal: 120–240 nm)- $z$  (vertical: 180–300 nm) plane 1.77 nm thick centered at  $y=174.53$  nm.

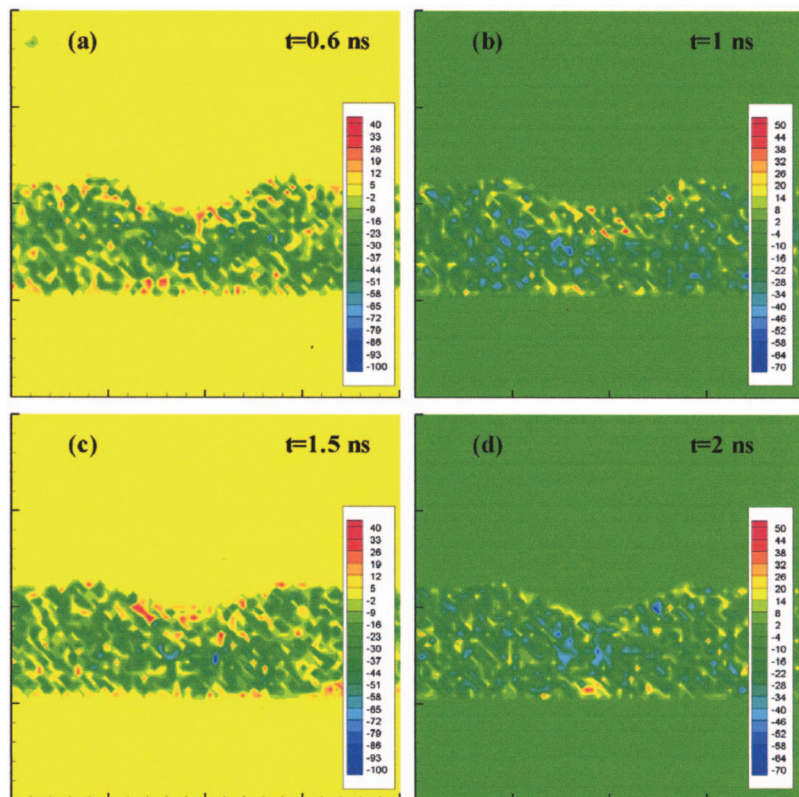


FIG. 7. (Color) Evolution of the stress component  $\sigma_{rr}$  in an  $x$  (horizontal: 120–240 nm)- $z$  (vertical: 180–300 nm) plane 1.77 nm thick centered at  $y = 174.53$  nm.

the latter stage of solidification, the solid-liquid interface becomes smaller, making the thermal transport from the liquid to solid weaker. In addition, the early stage thermal transport to the solid and the latent heat release to the solid due to solidification reduce the temperature difference between the solid and the liquid. This will lead to a reduced thermal transport from the liquid to the solid. Consequently, the liquid will have a smaller temperature reducing rate.

In our recent work,<sup>21</sup> detailed study was performed on the stress in surface nanostructuring with laser-assisted STM. The study was focused on the time duration before the solidification took place. It was found that the shear stress was much smaller than the normal stress and the three normal stresses ( $\sigma_{rr}$ ,  $\sigma_{\theta\theta}$ , and  $\sigma_{zz}$ ) shared the same propagation style in the  $x$ - $z$  planes. In this work, only the stress component  $\sigma_{rr}$  is plotted in Fig. 7. The local stress is calculated as<sup>21,29</sup>

$$\sigma_{mn} = -\frac{1}{\Delta V} \left( \sum_{i \neq j}^N r_{ij,m} F_{ij,n} + \delta_{mn} N k_B T \right). \quad (5)$$

In Eq. (5),  $\Delta V$  is the volume of a small domain of interest, and  $N k_B T$  is the stress induced by the translational movement of atoms. The local stress is averaged over a small domain with a size of about 1.7 nm. The other two normal stresses  $\sigma_{zz}$  and  $\sigma_{\theta\theta}$  follow the same evolution as shown in Fig. 7. At 0.6 ns, the normal stress in the liquid and the region adjacent to it is largely compressive, in the order of tens of megapascal. At 1 ns, the stress in the liquid is around zero. In some locations in the liquid, tensile stress is observed as well. More locations in the liquid have tensile stress at 1.5 ns. At this moment, in the solid part the stress is still compressive (negative). At 2 ns, the stress in the liquid is around zero although the tensile stress is observed at a few spots.

To obtain a better understanding of the stress evolution in the liquid, Fig. 8 shows the temporal change of six stresses ( $\sigma_{rr}$ ,  $\sigma_{\theta\theta}$ ,  $\sigma_{zz}$ ,  $\sigma_{rz}$ ,  $\sigma_{r\theta}$ , and  $\sigma_{\theta z}$ ) in the liquid. For each stress, the value displayed in Fig. 8 is an averaged number for the entire liquid. It is clear in Fig. 8 that the shear stresses are negligible in comparison with the normal stresses. The value of the shear stresses has a small fluctuation around zero and shows no visible trend of change with time. On the other hand, the three normal stresses experience a rapid decay in the early state of solidification. During most time of solidification, the normal stresses are compressive, meaning an internal pressure in the liquid.

It needs to be emphasized that for the temperature and stress distributions at 2 ns, no clear abnormal behavior is observed in the structural damage (atomic dislocation) region

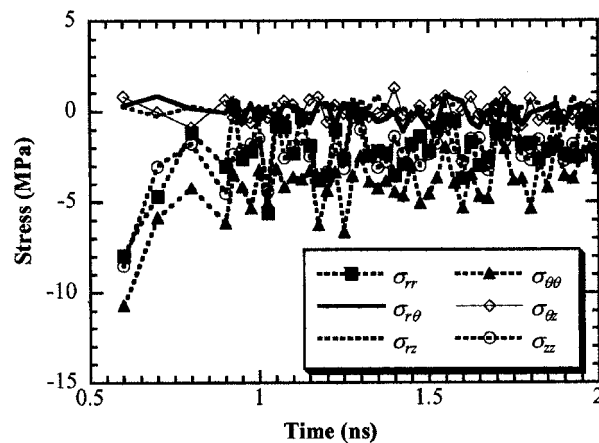


FIG. 8. Evolution of the average normal and shear stresses in the liquid during the solidification procedure.

marked in Figs. 3 and 4. Therefore, for the nanoscale structural damages formed in solidification, the local temperature and stress could not be appropriate parameters to identify the unique characteristics of the structural damage.

### C. Distinguishing of solid and liquid

The solidification described above is driven by the heat conduction in the material. Knowledge of the rate of solidification is important to understand how fast the nanostructuring procedure will finish. One direct way to measure the rate of solidification is how fast the volume of the liquid decreases with time. To characterize the volume reducing rate of the liquid, criteria have to be established to distinguish the liquid and solid. In our previous work,<sup>30</sup> the number density distribution of atoms in space was used to identify the solid-liquid interface. For two-dimensional (2D) and three-dimensional (3D) situations, this method becomes difficult to give accurate results.

In this work, we propose two functions to directly reflect the structure of the material and distinguish the liquid and solid. One function is

$$\Psi(r_{ij,x}) = \frac{1}{N(N-1)} \sum_{i \neq j} \left( r_{ij,x} - \frac{a}{2} \text{int} \left[ \frac{r_{ij,x}}{a/2} + 0.5 \right] \right)^2, \quad (6)$$

where  $r_{ij,x}$  is the distance between atoms  $i$  and  $j$  in the  $x$  direction,  $a$  is the lattice constant, and  $N$  is the number of atoms. The function  $\text{int}[x]$  in Eq. (6) is an integer function to take the integer part of the variable  $x$ . The physical meaning behind function (6) is that for perfect crystals,  $r_{ij,x}$  is equal to  $n(a/2)$ , leading to zero for  $\Psi$ . The extent of deviation of  $r_{ij,x}$  from  $n(a/2)$  reflects the crystallinity of the material.  $\Psi(r_{ij,x})$  is expected to have a much larger value in liquid than in crystal. In Eq. (6),  $r_{ij,y}$  and  $r_{ij,z}$  can also be used instead of  $r_{ij,x}$ .

The other function constructed is similar to the  $x$ -ray diffraction, but with a simpler definition of the crystallinity by taking advantage of numerical calculation. This function is designed as

$$\Phi(r_{i,z}) = \frac{1}{N} \left| \sum_i e^{j2\pi(2r_{i,z}/\lambda)} \right|, \quad (7)$$

where  $r_{i,z}$  is the  $z$  coordinate of the position of atom  $i$ ,  $N$  is the number of atoms within the domain of interest, and  $\lambda$  is the light wavelength. In this work,  $\lambda$  takes the value of the lattice constant  $a$ . In Eq. (7),  $2r_{i,z}$  is the distance light travels when it originates from  $z=0$ , reflected by the atom  $i$  at the location of  $r_{i,z}$ , and returns to the original location  $z=0$ . If atoms are regularly distributed in space with their spacing in the  $z$  direction equal to  $n(a/2)$ , the function  $\Phi(r_{i,z})$  will be equal to 1. In liquid, the function  $\Phi(r_{i,z})$  will be much less than 1.

Figure 9 shows the functions  $\Psi(r_{ij,x})$  and  $\Phi(r_{i,z})$  in a certain domain at  $t=1$  ns. It is evident that both functions work well in terms of distinguishing the solid and liquid regions. In the solid region,  $\Psi(r_{ij,x})$  is small, below  $4 \times 10^{-3}$ , showing the sound regularity of the crystal structure. On the other hand, in the liquid region, atoms are randomly distributed in space, and  $\Psi(r_{ij,x})$  becomes large, around 12

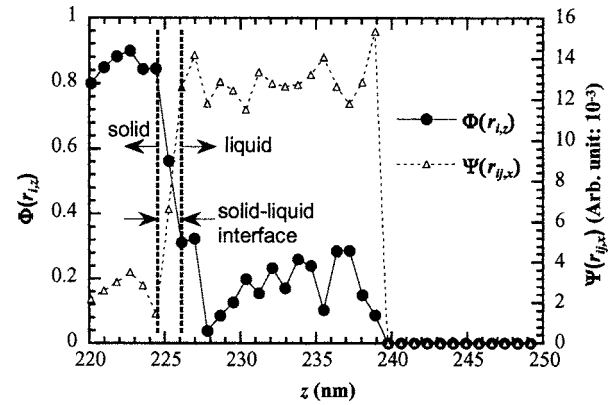


FIG. 9. Functions  $\Psi(r_{ij,x})$  and  $\Phi(r_{i,z})$  to demonstrate the solid and liquid structures as well as their interface. The domain under study is centered at  $x=175.41$  nm and  $y=174.53$  nm with  $\delta x=0.8515$  nm and  $\delta y=1.77$  nm at  $t=1$  ns.

$\times 10^{-3}$ . For the function  $\Phi(r_{i,z})$ , its value is large in the solid region, larger than 0.8. In the liquid region, the reflected light has weak diffraction, and  $\Phi(r_{i,z})$  becomes small, less than 0.3. In this work, the function  $\Phi(r_{i,z})$  is used to distinguish the solid and liquid regions and used for the analysis described below. Figure 10 shows the distribution of  $\Phi(r_{i,z})$  at different times in an  $x$ - $z$  plane. It is evident that the constructed function  $\Phi(r_{i,z})$  plays a sound role in terms of distinguishing the solid and liquid. In addition, it shows that in the solid region below the nanohole, the crystallinity ( $\Phi:0.8-0.9$ ) is not as good as that ( $\Phi:0.9-1$ ) in the region far from the nanohole. The possible reason for this phenomenon is that the region below the nanohole experiences slight deformation because of the phase explosion process during nanostructuring. For higher laser fluences, lattice bending was observed in the region adjacent to or below the nanohole.<sup>21</sup> At the solid-liquid interface, the value of  $\Phi(r_{i,z})$  is around 0.5. In this work, 0.5 is used as the criterion to identify the solid-liquid interface. At 1.5 and 2 ns, the distribution of  $\Phi(r_{i,z})$  clearly shows the atomic dislocation region. In this region, even the material is solid, the value of  $\Phi(r_{i,z})$  is around 0.5, much smaller than the typical value of  $\Phi(r_{i,z}) (>0.8)$  in crystal. It is conclusive that in this region, the regularity of the crystal structure is severely damaged by the atomic dislocation.

### D. Rate of solidification

Based on the observation in Fig. 10, one criterion is taken to distinguish the solid and liquid:  $\Phi(r_{i,z}) < 0.5$  for liquid and  $\Phi(r_{i,z}) > 0.5$  for solid. Employing this criterion, the number of atoms within the liquid as well as its volume are plotted out in Fig. 11. Within the time of study (0.6–2 ns), the volume of the liquid decays with time almost linearly, meaning the solidification rate is almost constant. Also plotted in Fig. 11 is the number density of the liquid in the unit of  $10/\text{nm}^3$ . It is evident that during the solidification procedure, the density of the liquid has a slight increase with time, probably due to the small temperature decay of the liquid as shown in Fig. 6. This density ( $\sim 20/\text{nm}^3$ ) is smaller than that of solid argon at 50 K ( $\sim 25.3/\text{nm}^3$ ).

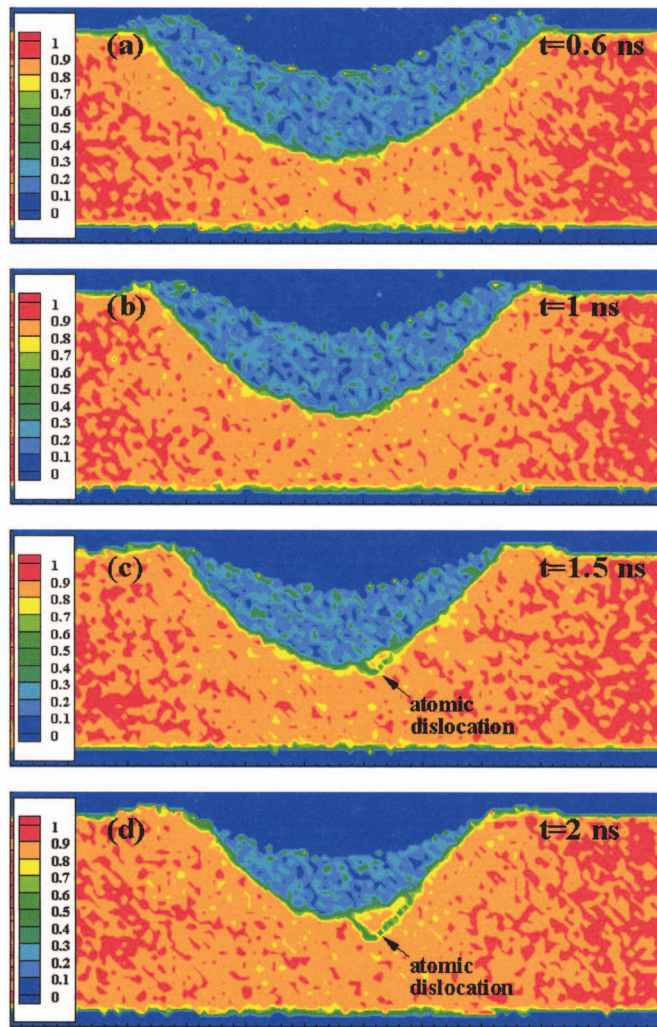


FIG. 10. (Color) The distribution of function  $\Phi(r_{i,z})$  at different times in an  $x$  (horizontal: 120–230 nm)- $z$  (vertical: 210–250 nm) plane 1.77 nm thick centered at  $y=174.53$  nm.

One important characteristic of the solidification procedure is the moving speed of the solid-liquid interface. This information is critical for estimating the time required to form the final surface nanostructure. In this work, the average moving speed of the solid-liquid interface is calculated by dividing the solid volume increasing rate with the area of

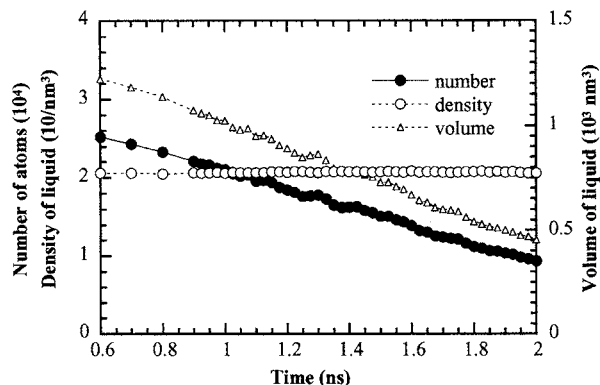


FIG. 11. Evolution of the number of atoms in the liquid as well as the volume of the liquid in an  $x$ - $z$  plane 1.77 nm thick centered at  $y=174.53$  nm.

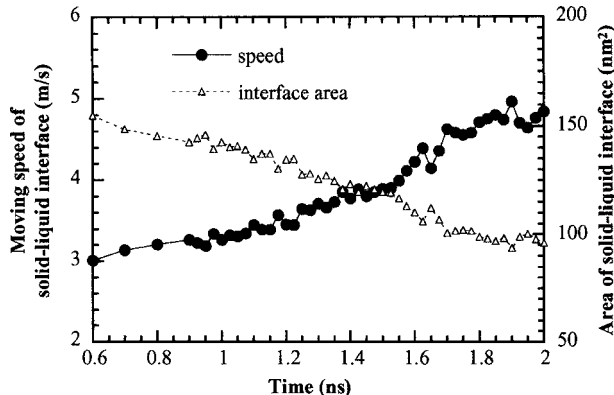


FIG. 12. Evolution of the moving speed and area of the solid-liquid interface. The domain under study is an  $x$ - $z$  plane 1.77 nm thick centered at  $y=174.53$  nm.

the solid-liquid interface. Figure 12 shows how the interface moving speed varies with time. Also plotted in Fig. 12 is the evolution of the interface area. It is observed that the interface speed increases with time from the initial 3 to 5 m/s at 2 ns. The solid-liquid interface moving speed is related to the local heat conduction rate as well the latent heat released in solidification. For the argon studied in this work, its thermal conductivity is small, in the order of 0.3 W/m K at 80 K. Attributed to this small thermal conductivity, the heat conduction rate in the material will be small, therefore leading to a slow solidification rate and solid-liquid interface moving speed. For materials used in practical experiment, the thermal conductivity is much larger than that of argon. It is expected a much faster solidification rate will result.

In addition to the average moving speed of the solid-liquid interface, the distribution of the moving speed in space is also important since this distribution strongly affects the final shape and structure in surface nanomanufacturing. Figure 13 shows the location of the solid-liquid interface determined using the criterion:  $\Phi(r_{i,z}) < 0.5$  for liquid and  $\Phi(r_{i,z}) > 0.5$ . It is found that the solid-liquid interface can be well fitted with a second-order polynomial curve. The fitting curves are shown in Fig. 13 as well, demonstrating a sound fitting result. When determining the local interface moving speed, instead of using the numerically determined interface

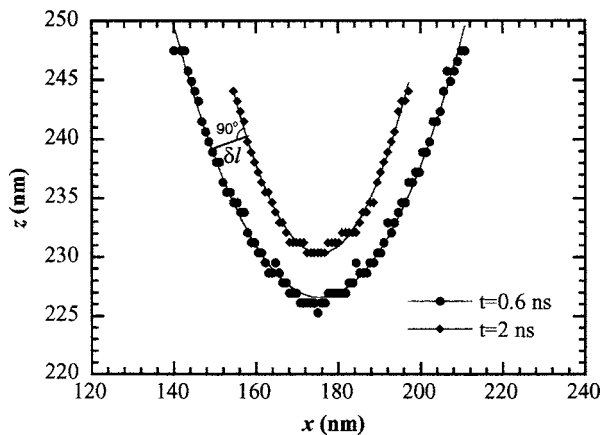


FIG. 13. Location of the solid-liquid interface at 0.6 and 2 ns, as well as the definition of the local solid-liquid interface moving speed.

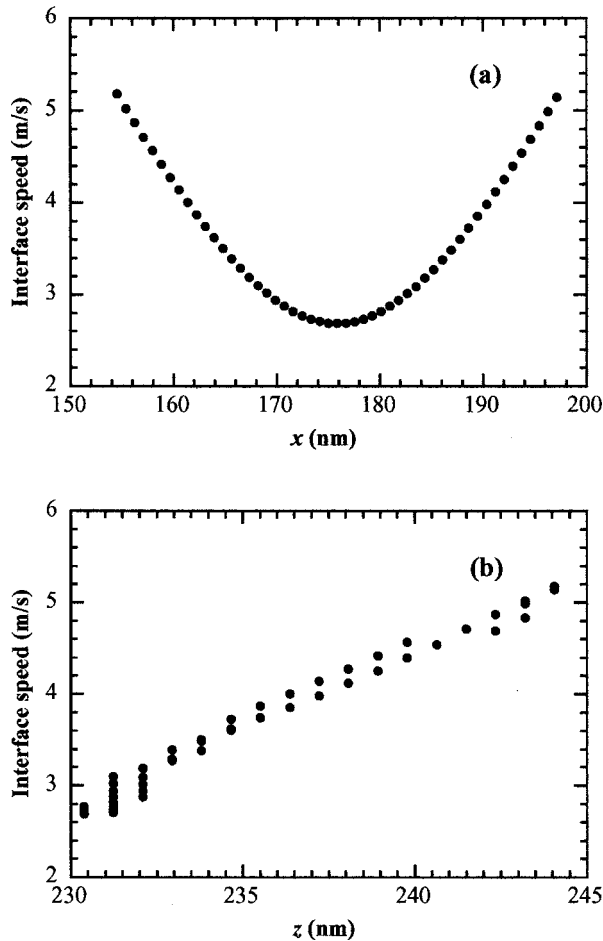


FIG. 14. The local moving speed of the solid-liquid interface: (a) distribution along the  $x$  coordinate and (b) distribution along the  $z$  coordinate.

location (solid points in Fig. 13), the fitting curve is used to suppress the statistical uncertainties. In the above average interface speed calculation, the area of the interface is also determined based on the fitting curves of the interfaces. When determining the local interface speed, a straight line is used to connect the interface at 0.6 and 2 ns. This line is normal to the local interface at 2 ns. The distance between the interfaces at 0.6 and 2 ns along this line ( $\delta l$ ) is divided by the elapsed time (1.4 ns) to obtain the local speed.

Figure 14 shows the local speed of the solid-liquid interface versus the location of the interface at 2 ns. Three conclusions can be drawn about the distribution of the local interface speed. First, the moving speed of the solid-liquid interface is nonuniform in space. The interface moves slower in the center than at the edge. Second, based on the distribution shown in Fig. 14(b), it is interesting to note that the interface moving speed has a linear distribution with respect to the height of the solid-liquid interface. It demonstrates that the liquid at the bottom of the hole solidifies slower than that at the edge. Finally, both Figs. 14(a) and 14(b) show that the moving speed of the solid-liquid interface is axis symmetrical, probably due to the early stage axis symmetrical heating by the enhanced optical field.

#### IV. CONCLUSION

In this work, large-scale molecular-dynamics simulation was conducted to study the long-time (up to 2 ns) behavior

of argon crystal in surface nanostructuring with laser-assisted STM. The research was focused on the solidification of the liquid. Epitaxial regrowth was observed in the solidification. Thermal strain-induced structural damage-atomic dislocation was observed in the epitaxial regrowth. During solidification, the melt was featured with decaying normal compressive stresses and negligible shear stresses. Two functions were designed and constructed to reflect the crystallinity and distinguish solid and liquid. The distribution of  $\Phi(r_{i,z})$  in space clearly showed the solid and liquid regions, their interface, as well as the thermal strain-induced atomic dislocation. Our study of the movement of the solid-liquid interface revealed an average moving speed of 3–5 m/s which increased with the time. The spatial distribution of the moving speed at the solid-liquid interface revealed nonuniform epitaxial regrowth in space. The liquid at the bottom of the nanohole solidified slower than that at the edge.

#### ACKNOWLEDGMENTS

Supports for this work from NSF (CTS: 0400458) and Nebraska Research Initiative are gratefully acknowledged. One of the authors (X.W.) thanks the strong support from Dr. David Y. S. Lou and the Department of Mechanical Engineering at UNL for the establishment of the parallel computer used for this work.

- <sup>1</sup>Y. F. Lu, Z. H. Mai, and W. K. Chim, *Jpn. J. Appl. Phys., Part 1* **38**, 5910 (1999).
- <sup>2</sup>J. Jersch, F. Demming, and K. Dickmann, *Appl. Phys. A: Mater. Sci. Process.* **A64**, 29 (1997).
- <sup>3</sup>Y. F. Lu, Z. H. Mai, Y. W. Zheng, and W. D. Song, *Appl. Phys. Lett.* **76**, 1200 (2000).
- <sup>4</sup>Y. F. Lu, B. Hu, Z. H. Mai, W. J. Wang, W. K. Chim, and T. C. Chong, *Jpn. J. Appl. Phys., Part 1* **40**, 4395 (2001).
- <sup>5</sup>J. Jersch and K. Dickmann, *Appl. Phys. Lett.* **68**, 868 (1996).
- <sup>6</sup>J. Jersch, F. Demming, L. J. Hildenhagen, and K. Dickmann, *Appl. Phys. A: Mater. Sci. Process.* **A66**, 29 (1998).
- <sup>7</sup>Y. F. Lu, Z. H. Mai, G. Qiu, and W. K. Chim, *Appl. Phys. Lett.* **75**, 2359 (1999).
- <sup>8</sup>B. Hu, Y. F. Lu, Z. H. Mai, W. D. Song, and W. K. Chim, *Proc. SPIE* **4088**, 232 (2000).
- <sup>9</sup>Z. H. Mai, Y. F. Lu, S. M. Huang, W. K. Chim, and J. S. Pan, *J. Vac. Sci. Technol. B* **18**, 1853 (2000).
- <sup>10</sup>Z. H. Mai, Y. F. Lu, W. D. Song, and W. K. Chim, *Appl. Surf. Sci.* **154–155**, 360 (2000).
- <sup>11</sup>A. Chimmalgi, T. Choi, and C. P. Grigoropoulos, *Proceedings of the 2002 ASME International Mechanical Engineering Congress and Exposition*, New Orleans, LA, 2002 (American Society of Mechanical Engineers, New York, 2002), pp. 291–295.
- <sup>12</sup>S. M. Huang, M. H. Hong, Y. F. Lu, B. S. Lukyanchuk, W. D. Song, and T. C. Chong, *J. Appl. Phys.* **91**, 3268 (2002).
- <sup>13</sup>S. Grafström, *J. Appl. Phys.* **91**, 1717 (2002).
- <sup>14</sup>W. Denk and D. W. Pohl, *J. Vac. Sci. Technol. B* **9**, 510 (1991).
- <sup>15</sup>O. J. F. Martin, C. Girard, and A. Dereux, *Phys. Rev. Lett.* **74**, 526 (1995).
- <sup>16</sup>A. Madrazo, M. Nieto-Vesperinas, and N. García, *Phys. Rev. B* **53**, 3654 (1996).
- <sup>17</sup>O. J. F. Martin and C. Girard, *Appl. Phys. Lett.* **70**, 705 (1997).
- <sup>18</sup>F. Demming, J. Jersch, K. Dickmann, and P. I. Geshev, *Appl. Phys. B: Lasers Opt.* **B66**, 593 (1998).
- <sup>19</sup>P. I. Geshev, F. Demming, J. Jersch, and K. Dickmann, *Appl. Phys. B: Lasers Opt.* **B70**, 91 (2000).
- <sup>20</sup>P. I. Geshev, F. Demming, J. Jersch, and K. Dickmann, *Thin Solid Films* **368**, 156 (2000).
- <sup>21</sup>X. Wang, *J. Phys. D* **38**, 1805 (2005).
- <sup>22</sup>D. Humbird and D. B. Graves, *Pure Appl. Chem.* **74**, 419 (2002).
- <sup>23</sup>C. S. Liu, Z. G. Zhu, J. Xia, and D. Y. Sun, *J. Phys.: Condens. Matter* **13**, 1873 (2001).

<sup>24</sup>Y. Chen, J. Zhang, and L. Wang, *Mater. Lett.* **59**, 676 (2005).

<sup>25</sup>F. F. Chen, H. F. Zhang, F. X. Qin, and Z. Q. Hu, *J. Chem. Phys.* **120**, 1826 (2004).

<sup>26</sup>X. Wang and X. Xu, *Int. J. Heat Mass Transfer* **46**, 45 (2003).

<sup>27</sup>M. P. Allen and D. J. Tildesley, *Computer Simulation of Liquids* (Clarendon, Oxford, 1987).

<sup>28</sup>X. Wang and C. Lawrence, *Proceedings of the ASME Heat Transfer/Fluids Engineering Summer Conference 2004*, Charlotte, NC, 2004 (American Society of Mechanical Engineers, New York, 2004), pp. 619–625.

<sup>29</sup>X. Wang, *J. Heat Transfer* **126**, 355 (2004).

<sup>30</sup>X. Wang and X. Xu, *J. Heat Transfer* **124**, 265 (2002).